ACS APPLIED MATERIALS & INTERFACES

www.acsami.org

Research Article

Direct Identification of Antisite Cation Intermixing and Correlation with Electronic Conduction in $CuBi_2O_4$ for Photocathodes

Hyun Joon Jung, Younghwan Lim, Byeong-Uk Choi, Hyung Bin Bae, WooChul Jung, Sangwoo Ryu, Jihun Oh, and Sung-Yoon Chung*

Cite This: *ACS Appl. Mater. Interfaces* 2020, 12, 43720–43727

Read Online

ACCESS | Metrics & More | Article Recommendations | Supporting Information

ABSTRACT: Cu-based p-type semiconducting oxides have been sought for water-reduction photocathodes to enhance the energy-conversion efficiency in photoelectrochemical cells. $CuBi_2O_4$ has recently attracted notable attention as a new family of p-type oxides, based on its adequate band gap. Although the identification of a major defect structure should be the first step toward understanding the electronic conduction behavior, no direct experimental analysis has been carried out yet. Using atomic-scale scanning transmission electron microscopy together with chemical probing, we identify a substantial amount of Bi_{Cu}–Cu_{Bi} antisite intermixing as a major point-defect type. Our density functional theory calculations also show that antisite Bi_{Cu} can seriously hinder the hole-polaron hopping between Cu, in agreement with lower conductivity and a larger thermal activation barrier under a higher degree of intermixing. These findings highlight the value of the direct identification of point defects for a better understanding of electronic properties in complex oxides.

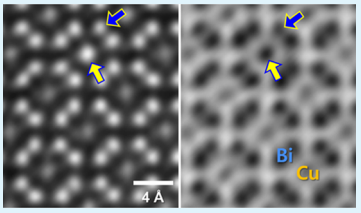

KEYWORDS: *antisite defects, copper oxides, EDS, photocathodes, p-type oxides, polaron hopping, STEM*

INTRODUCTION

As in many electrochemical energy-conversion devices, photoelectrochemical (PEC) cells consist of two major electrodes for hydrogen fuel generation via solar water splitting on a large scale. As hydrogen- and oxygen-evolution reactions for water reduction and oxidation take place at the interface between the photoelectrodes and the electrolyte in a PEC cell,[1] the selection of optimum materials for the electrodes and their subsequent design for better solar-to-hydrogen conversion efficiency have been central issues in the relevant fields.[2−6] In particular, highly alkaline (pH > 12) or acidic (pH < 5) aqueous solutions are usually utilized as an electrolyte for more efficient water splitting in the cells. Since the milestone work on TiO_2 by Fujishima and Honda,[7] a number of semiconducting oxides, which are considered to be chemically more stable than covalently bonded traditional semiconductors, thus have been sought for photoelectrodes with better chemical stability and electron–hole separation as well as adequate band gaps and charge-transport properties.[5,6]

There are two generally attainable approaches to prepare semiconducting oxides having an n-type conductivity from a defect chemical viewpoint. One is the utilization of a small amount of donor dopants so that their charge compensation should be made by electrons ($[D^{\bullet}] = e'$, where $D^{\bullet}$ denotes the donor dopants with an effectively positive charge). The other is annealing oxides under sufficiently low oxygen partial pressure to create oxygen vacancies and subsequent charge-compensating electrons ($2[V_O^{\bullet\bullet}] = e'$). As a result, in addition to TiO_2, many other n-type oxide candidates have been experimentally demonstrated to show notable performance as photoanodes for oxygen evolution.[5,8−10] In stark contrast, the preparation of p-type oxides is comparatively challenging. Even if acceptor dopants are added, their charge compensation is usually achieved through the formation of oxygen vacancies ($[A'] = 2[V_O^{\bullet\bullet}]$, where A′ denotes acceptor dopants with effectively negative charge) rather than holes, unless the oxygen partial pressure during annealing is remarkably high. In this regard, Cu-based oxides,[6,11] most of which have a 3d9 (Cu^{2+}) or 3d10 (Cu^{1+}) electronic configuration for plausible hole conduction in the 3d orbitals, are an important family of oxide materials showing a p-type behavior.

A p-type ternary $CuBi_2O_4$ was first identified as a new potential candidate for the photocathode in 2007.[12,13] While recent studies systematically reported various electrical and electrochemical properties of $CuBi_2O_4$,[14−20] the basic defect structures, which strongly correlate with the overall electronic transport behavior, have not been experimentally demonstrated. As already shown in other well-known p-type transition-metal oxides such as FeO, NiO, and CoO, Cu cation vacancies were suggested to be the origin of the hole formation ($2[V_{Cu}''] = h^{\bullet}$).[16,19] Although Cu vacancies appear to be reasonable point defects to explain the p-type conduction behavior, no experimental direct observation has been made

Received: July 10, 2020
Accepted: September 2, 2020
Published: September 2, 2020

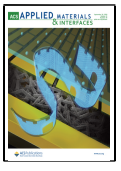

https://dx.doi.org/10.1021/acsami.0c12491
ACS Appl. Mater. Interfaces 2020, 12, 43720–43727

yet to elucidate the defect structures at an atomic scale in $CuBi_2O_4$. Although it is fairly challenging, atomic-level scrutiny to identify possible defect chemical equilibria should be the first step toward a precise understanding of the electrical conduction, particularly in complex oxides with multiple cations.

In this work, by utilizing atomic-column-resolved scanning transmission electron microscopy (STEM)[21−28] along with atomic-level energy-dispersive X-ray spectroscopy (EDS),[24,29,30] we directly identify the presence of a substantial amount of antisite defects, Bi_{Cu} and Cu_{Bi}, in $CuBi_2O_4$ thin films. From a comparison with image simulations, we further found that their presence is not locally confined but prevails over the entire crystals as one of the major point defects. A combination of optical and electrical measurements and density functional theory (DFT) calculations demonstrates that the thermally activated electronic conductivity increment may be associated with small polaron hopping along the *c*-axis between neighboring Cu^{2+}, the local 3d states of which appear near the valence band edge in the band gap, in agreement with previous reports on many polaron-conducting oxides.[31,37] Suggesting a new possible conduction mechanism by hole polarons in line with the crystal structure, our direct and statistical STEM analysis together with DFT calculations shows that the overall electronic transport in $CuBi_2O_4$ can be remarkably affected by antisite intermixing, although complete suppression of intermixing is likely to be fairly difficult to achieve.

RESULTS AND DISCUSSION

It is noted that $CuBi_2O_4$ has a fairly peculiar crystal structure, although its chemical formula is identical to that of AB_2O_4-type spinel oxides. The illustrations in Figure 1a,b show its crystal structure in the *c*-axis and *b*-axis projections, respectively. The basic $CuBi_2O_4$ structure consists of a square-planar $[CuO_4]$ connected by Bi cations (Figure 1a), and the planar $[CuO_4]$ units are stacked along the *c*-axis (Figure 1b). Each of the $[CuO_4]$ and $[BiO_4]$ units is also described separately in Figure 1c. As delineated without Bi in Figure 1d, the unique structure of $CuBi_2O_4$ is therefore based on the completely isolated square-planar $[CuO_4]$ (see Supporting Movie S1 for the three-dimensional illustration), while many other oxides are composed of oxygen octahedra and tetrahedra with a corner- or edge-sharing configuration in general. The significant correlation of these structural characteristics with the electronic conduction behavior will be discussed in detail below.

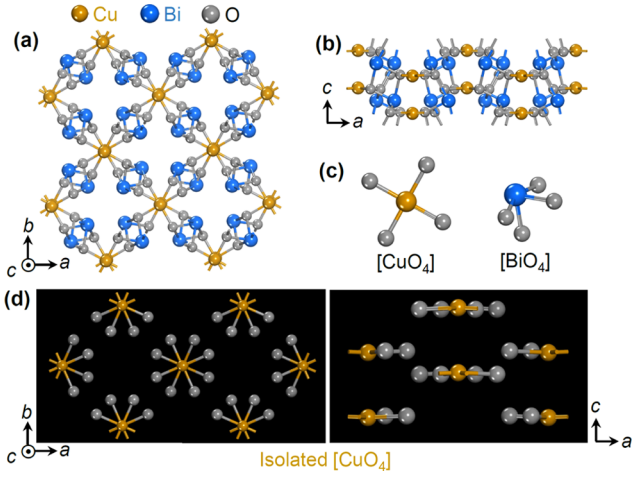

Figure 1. Crystal structure of $CuBi_2O_4$. (a) This illustration schematically describes the atomic configuration in the *c*-axis projection, showing the square-planar $[CuO_4]$ units connected by Bi. (b) Structure is shown in the *b*-axis projection. The planar $[CuO_4]$ units are easily recognized to be stacked along the *c*-axis. (c) Individual $[CuO_4]$ and $[BiO_4]$ subunits are presented. (d) A set of illustrations in both *c*- and *b*-axis projections is depicted without Bi. Three-dimensionally isolated $[CuO_4]$ square planes are readily identifiable as a notable structural feature.

Polycrystalline $CuBi_2O_4$ thin films were fabricated by a sol−gel process.[20] As demonstrated in Figure 2a, a plane-view scanning electron microscopy (SEM) image shows that polycrystalline dense $CuBi_2O_4$ thin films (~300 nm thickness) are successfully prepared by a sol−gel process (see Figure S1 of the Supporting Information for SEM images and X-ray diffraction patterns). The most striking feature of the atomic-scale STEM analysis is that notably high-intensity Cu columns are frequently observed. The yellow arrows on the high-angle annular dark-field (HAADF) STEM image (left) in Figure 2b exemplify one of the Cu columns that exhibit remarkably high intensity. Because the thin-film sample is pristine and stoichiometric without any dopants, such high-intensity Cu columns directly indicate the presence of antisite Bi at the Cu sites, "Bi_{Cu}". Note that the atomic number (Z) of Bi is much higher than that of Cu (Z_{Bi} = 83 and Z_{Cu} = 29). As a result, the antisite Bi_{Cu} is readily identifiable in the *Z*-contrast HAADF mode. A counterpart bright-field (BF) image is also provided in the right-hand column in Figure 2b, showing the inverse black-and-white image contrast.

As aforementioned, our thin-film sample is pristine and stoichiometric. Therefore, if antisite Bi exists, antisite Cu at the Bi sites should be accompanied at the same time. Indeed, when we observed the lattice at a higher magnification, we could identify the presence of antisite Cu_{Bi}, as denoted by blue arrows in Figure 2c. It is worth clarifying that the number of Bi sites in the unit cell of $CuBi_2O_4$ is double the number of Cu sites. Consequently, if pairs of antisite defects, Bi_{Cu} and Cu_{Bi}, are created, the intensity of Bi columns will be influenced much less by antisite Cu_{Bi}, compared with the intensity of Cu columns by antisite Bi_{Cu}. In this sense, while the high-intensity Cu columns by antisite Bi_{Cu} are easily probed during the STEM observation, Bi columns showing a comparatively lower intensity by antisite Cu_{Bi} are not very easily identifiable. Nevertheless, the STEM images in Figure 2c, in particular the BF image, provide direct evidence of the pair of antisite defects, Bi_{Cu} (yellow arrow) and Cu_{Bi} (blue arrow) in $CuBi_2O_4$. To clarify the contrast variation by Cu_{Bi}, the reverse intensity of the two Bi columns in the BF image is compared in Figure 2d, showing the intensity reduction. An additional pair of wide-view HAADF- and BF-STEM images is provided in Supporting Information Figure S2 to show the consistent image feature.

To quantify the degree of antisite cation intermixing, we carried out STEM image simulations based on the multislice method.[24,38−40] Figure 3a shows a series of simulated HAADF images in the [001] projection together with the profiles of Cu- and Bi-column intensities, as indicated by yellow broken lines. The first image on the top represents the atomic column contrast for the pristine $CuBi_2O_4$ lattice. As the column intensity in a *Z*-contrast HAADF image is proportional to $\sim Z^2$ of a column,[41] the relative intensity of Cu columns is notably low, as verified in the intensity profile. The remaining three

https://dx.doi.org/10.1021/acsami.0c12491
ACS Appl. Mater. Interfaces 2020, 12, 43720−43727

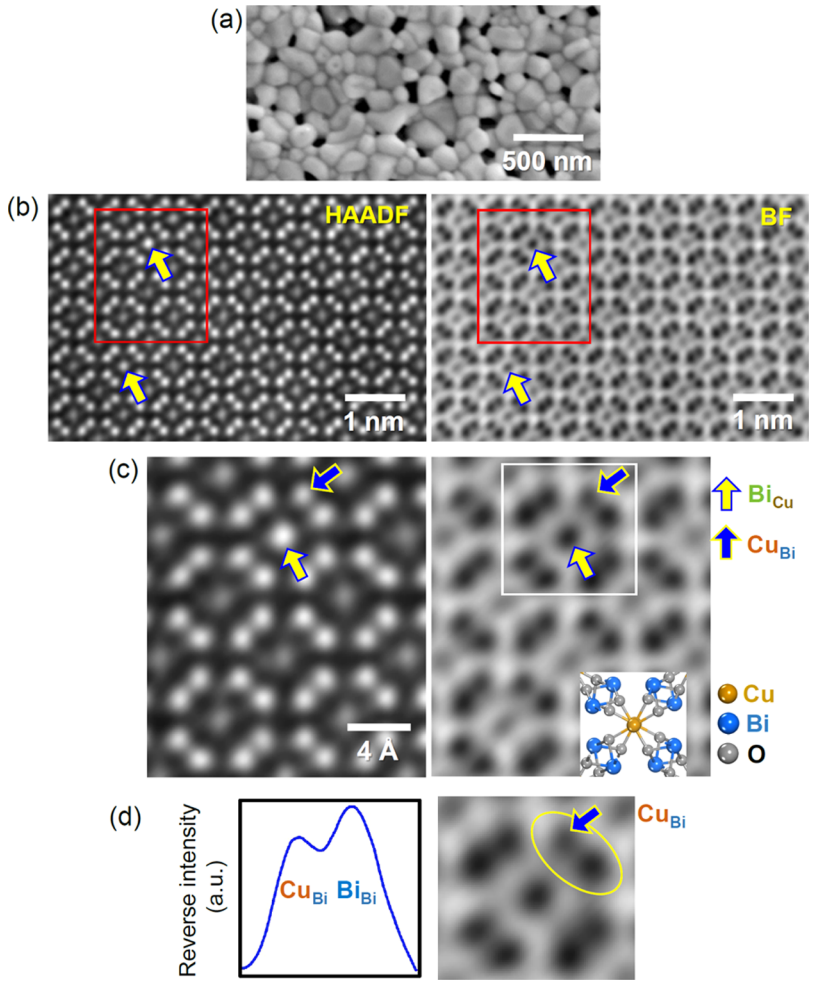

Figure 2. Identification of antisite defects. (a) Polycrystalline microstructure of a $CuBi_2O_4$ film is shown in a plane-view SEM image. (b) A pair of atomic-scale HAADF and BF images is provided. As indicated by yellow arrows, substantially high intensity is observed in some Cu columns during the STEM analysis. (c) This pair of enlargements for the location denoted by a red rectangle in (b) reveals both a higher-intensity Cu column (yellow arrow) and a lower-intensity Bi column (blue arrow), indicating the presence of Bi_{Cu}−Cu_{Bi} antisite intermixing. The lower-intensity Bi column is easily distinguishable in the BF image. (d) A BF image more sensitively visualizes the contrast variation by antisite Cu_{Bi} than an annular dark-field (ADF) image does. A reverse column-intensity profile is provided to clarify the presence of Cu_{Bi}, as indicated by a blue arrow in the enlarged BF image.

simulated images in Figure 3b were acquired for different degrees of Cu−Bi intermixing. Cases 1−3 demonstrate the [001] lattice images of $(Cu_{0.96}Bi_{0.04})(Bi_{1.96}Cu_{0.04})O_4$, $(Cu_{0.92}Bi_{0.08})(Bi_{1.92}Cu_{0.08})O_4$, and $(Cu_{0.84}Bi_{0.16})(Bi_{1.84}Cu_{0.16})$-$O_4$, respectively. During image simulation, the intensity of the Bi columns was set to be constant in each case. As directly revealed in each intensity profile below the simulated images, the relative intensity of Cu columns (yellow arrows) becomes higher with an increasing degree of Cu−Bi intermixing.

When we compared the simulated image for pristine $CuBi_2O_4$ with experimentally obtained images, we could readily recognize that the intensity of most Cu columns in the real images is substantially higher than the Cu-column intensity acquired from the simulation. An experimental HAADF image and the simulated image (in color) in Figure 3c provide direct evidence of the significantly higher intensity of Cu columns in the real image obtained for a thin-film sample fabricated at 550 °C. For a statistical and quantitative treatment, we measured the relative intensities of more than 350 pairs of Cu columns and their nearest Bi columns, as exemplified by a blue oval on the image. The bar graph in Figure 3c plots the distribution of the relative Bi/Cu intensities of the pairs. Based on the simulation for pristine $CuBi_2O_4$, the Bi/Cu intensity ratio should be 4.25 (see the green vertical line on the bar graph). However, the average Bi/Cu intensity ratio measured from the experimental HAAADF image is 3.3, as indicated by a black broken line on the bar graph, directly verifying the Cu−Bi intermixing. This value of the Bi/Cu intensity ratio (3.3) corresponds to ∼6% intermixing in terms of the Cu sites, the composition of which is $(Cu_{0.94}Bi_{0.06})$-$(Bi_{1.94}Cu_{0.06})O_4$. Figure 3d also shows a set of image comparisons and the results of the Bi/Cu intensity ratios measured from a thin-film sample fabricated at 750 °C. As can be noticed in the bar graph, the average Bi/Cu intensity ratio of the 750 °C sample is much lower (2.6), exhibiting a higher degree of intermixing (∼10% in terms of the Cu sites) than that of the 550 °C sample. It is also worth mentioning that some pairs have the Bi/Cu intensity ratio higher than 4.25. This implies that Cu vacancies are present at the Cu columns in addition to Cu−Bi intermixing, resulting in a comparatively lower intensity in the Cu columns. However, as pairs of Cu−Bi columns having a higher Bi/Cu ratio than 4.25 are hardly

https://dx.doi.org/10.1021/acsami.0c12491
ACS Appl. Mater. Interfaces 2020, 12, 43720−43727

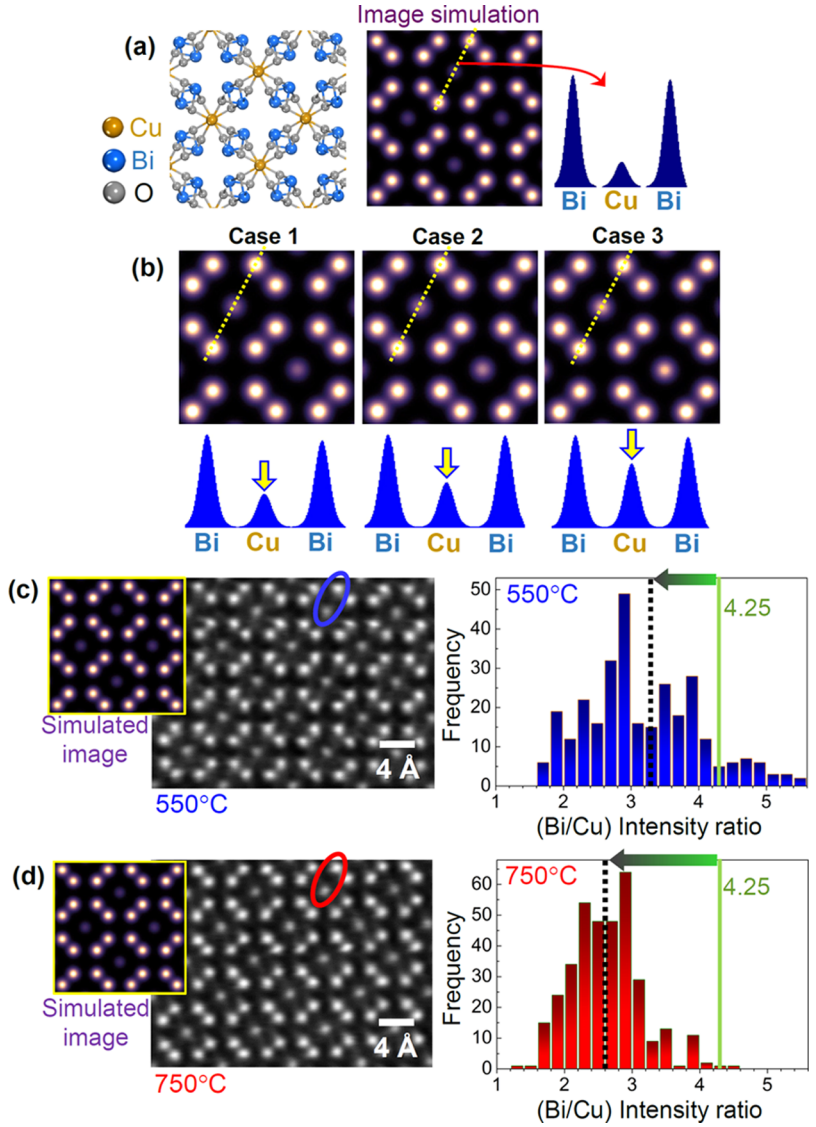

Figure 3. HAADF image simulations and comparison with real images. (a) A simulated HAADF image in the [001] projection shows eight very bright Bi columns around each comparatively much lower-intensity Cu column. A quantitative intensity profile is also provided for the Bi−Cu−Bi column denoted by a yellow broken line. (b) A series of simulated HAADF images are demonstrated with different degrees of intermixing: $(Cu_{0.96}Bi_{0.04})(Bi_{1.96}Cu_{0.04})O_4$, $(Cu_{0.92}Bi_{0.08})(Bi_{1.92}Cu_{0.08})O_4$, and $(Cu_{0.84}Bi_{0.16})(Bi_{1.84}Cu_{0.16})O_4$ for cases 1−3, respectively. The intensity of the Cu column in the series of profiles is noted to become higher with increasing the intermixing degree. (c) Most Cu columns in the image are much brighter than those in the simulated image (in color) in the 550 °C film sample. The bar graph statistically shows the distribution of Bi/Cu intensity ratios. A lower average ratio (3.3, black broken line) than the ratio (4.25, green vertical line) estimated from the simulation without intermixing is noted. (d) The analogous image feature showing bright Cu columns is identified in a 750 °C film. A much lower value for the average Bi/Cu intensity ratio (2.6, black broken line) is presented in the bar graph, demonstrating a higher degree of intermixing.

found in the 750 °C sample (Figure 3d), the formation of Cu vacancies is likely to be metastable at low temperature, finally being suppressed at a high-temperature equilibrium state.

In addition to the statistical and quantitative image simulations and subsequent comparison, we performed an atomic-scale EDS compositional analysis to consolidate the presence of antisite intermixing as one of the major point defects in $CuBi_2O_4$. Two sets of EDS maps obtained in the 750 °C sample are provided in Figure 4, chemically visualizing the Cu and Bi sites at an atomic level. More importantly, as indicated by arrows in each of the maps, both significant X-ray signal of Bi in the Cu sites (see the Bi maps) and a signal of Cu in the Bi sites (see the Cu maps) could be detected above the background noise, clearly verifying the presence of antisite intermixing by chemical evidence. Another set of EDS maps is provided in Supporting Information Figures S3 and S4 at higher magnification for confirmation.

Based on previous reports on $CuBi_2O_4$ films, its optical band gap is known to be 1.6−1.8 eV. The optical absorbance measurements for our films to acquire the Tauc plots also consistently agree well with the previously reported results, showing that the band gap is 1.75 eV for the 550 °C sample and 1.74 eV for the 750 °C sample, as provided in the Tauc plots in Figure 5a (see Supporting Information Figure S5 for the optical absorbance measurements of the films). In stark contrast, the thermal activation barrier for electronic conduction completely differs from these values of the optical band gap. The Arrhenius plots in Figure 5b demonstrate that the activation energy (the slope of each plot) is notably as small as 0.27 and 0.31 eV for the 550 and 750 °C samples,

https://dx.doi.org/10.1021/acsami.0c12491
ACS Appl. Mater. Interfaces 2020, 12, 43720−43727

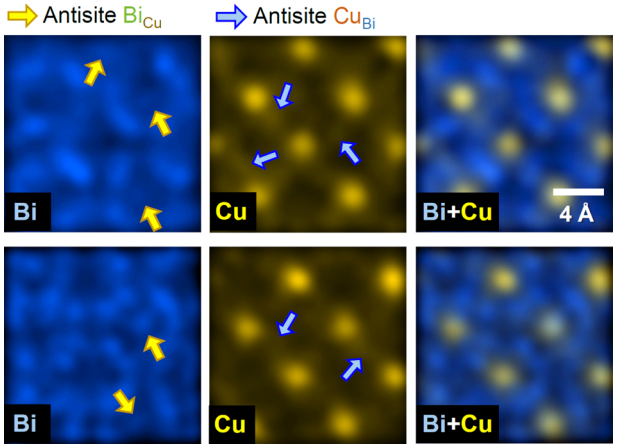

Figure 4. Atomic-level EDS mapping. The maps were acquired in the 750 °C film sample. Yellow arrows in the Bi maps indicate the presence of Bi_{Cu} antisite defects. Light blue arrows in the Cu maps also exemplify Cu_{Bi} antisite defects. This set of maps provide compelling chemical evidence proving a substantial degree of cation intermixing.

respectively. This implies that the increment of electronic conductivity with temperature in $CuBi_2O_4$ is not associated with the simple intrinsic electron−hole pair generation as observed in Si-based semiconductors. Consequently, precisely investigating the electronic structure of $CuBi_2O_4$ by taking into consideration the antisite defects appears to be a necessary step to understand the discrepancy between the optical band gap and the thermal activation energy for electrical conduction.

Ab initio DFT calculations were carried out to scrutinize the electronic band structure and the density of states (DOS) with and without antisite intermixing. To consider the strong electron-exchange correlation of the Cu 3d states, the Hubbard U parameter was employed (U = 7 eV for Cu 3d states)[42−44] along with a sufficiently large plane-wave basis set for the kinetic energy cutoff (1000 eV) for better accuracy during the calculations. Figure 5c shows the DOS and the electronic band diagram of pristine $CuBi_2O_4$. As observed in many other first-row transition-metal oxides, the valence band of $CuBi_2O_4$ is composed of the hybridization of the Cu 3d (orange curves) and O 2p (gray curves) orbitals, while the conduction band largely consists of the Bi 6p (blue curves) orbital. In addition, an indirect band gap (E_g) was obtained from our GGA + U method in the DFT calculations (see Supporting Information Figure S6), showing E_g = 1.68 eV, as indicated by a green arrow in the band structure. This calculated band gap is noted to be consistent with the gap acquired from the Tauc plots (Figure 5a) by the optical absorbance measurements.

One of the most noticeable features in the electronic structure of $CuBi_2O_4$ is that there is an additional small DOS within the band gap. A black arrow together with a gray shadow in the DOS plot and the band diagram indicates these local electron states. As already consistently demonstrated in $LiFePO_4$,[32] electron-doped $BiVO_4$,[33] Li_2FeSiO_4,[34] and doped Fe_2O_3[35−37] through DFT calculations (see Supporting Information Figure S7 for examples), the presence of such local states within the band gap is a crucial indication of the small polaron states. In particular, these local states are confined to a much narrower energy width near the valence band maximum, when cation intermixing by the antisite defect pairs (Bi_{Cu} (green sphere) and Cu_{Bi} (light red sphere) in the illustration) is introduced in the supercell, as shown in the DOS and the band structure in Figure 5d. Two DOS plots in Figure 5e compare the distinct contributions of the Cu 3d states from insite Cu_{Cu} and antisite Cu_{Bi}. While a large amount of the 3d states of insite Cu make a significant contribution to the polaron states (gray shadow), most of the 3d states of antisite Cu place within the valence band, constructing a major d-orbital component at the valence band edge, as denoted by a yellow shadow. Consequently, although the band gap is hardly affected by the presence of antisite intermixing, the polaron states in addition to the valence band edge appear to considerably vary with antisite intermixing. In addition, the indirect band gap shown in pristine $CuBi_2O_4$ was changed to be the Γ-point direct band gap in defective $CuBi_2O_4$ with intermixing (see Supporting Information Figure S6). It is also worthwhile to mention that a previous DFT study under a much smaller plane-wave basis set for the kinetic energy cutoff (400 eV) and a different U value for Cu does not show any local polaron states in the electronic band structure, although we verified that the presence of these local states within the band gap was not affected even under the calculation conditions that the previous study applied.

By atomic-scale physical imaging and chemical probing, our study clarifies that more than 5% Cu exchange with Bi as one of the major prevailing point defects in $CuBi_2O_4$ thin films. Along with this direct observation, a combination of optical absorbance and thermally activated conductivity measurements and DFT calculations consistently demonstrates that the overall conduction is likely to be achieved largely by small hole polarons in $CuBi_2O_4$ containing antisite defects. Moreover, as illustrated in Figure 1 and Supporting Information Movie S1, the [CuO_4] square planes, which are key structural units for the valence band, are noted to be completely isolated from each other. Therefore, the isosurface of an electronic density difference field shown in Figure 6a is mostly confined to Cu and O, revealing no charge distribution around Bi. Unless the Bi 6s orbital was strongly coupled with the hybridization of Cu 3d and O 2p states, it appears from the structural viewpoint that the simple bandlike hole conduction in the valence band would not be easily achievable in pristine $CuBi_2O_4$ with no intermixing.

Figure 6b shows the electron-density isosurface in the b-axis projection. As noted in the figure, the nearest cation of Cu is another Cu along the c-axis, showing that the distance of Cu−Bi (3.24 and 3.62 Å) is longer than that of Cu−Cu (2.96 Å) in the unit cell. The hole-polaron hopping between Cu atoms along the c-axis thus can be a valid conduction mechanism in this structural sense as well. In contrast, if substantial cation intermixing is unavoidable, the isolated [CuO_4] square planes can be connected by antisite Cu_{Bi} and subsequently the 3d states of antisite Cu_{Bi} make a notable contribution to the valence band, as already shown in Figure 5e. Although the present study shows that the width of the polaron states within the band gap becomes narrower by antisite intermixing, the electrical conduction by the small polarons is likely to remain as a substantial mechanism in $CuBi_2O_4$. As noted in the Arrhenius plots in Figure 5b, both a larger activation barrier (0.31 eV) and a lower electronic conductivity observed in the 750 °C sample with a higher degree of Cu−Bi intermixing are thus reasonably understood, as polaron hopping along the c-axis can be seriously blocked by antisite Bi_{Cu}, hardly contributing to the local polaron states.

https://dx.doi.org/10.1021/acsami.0c12491
ACS Appl. Mater. Interfaces 2020, 12, 43720−43727

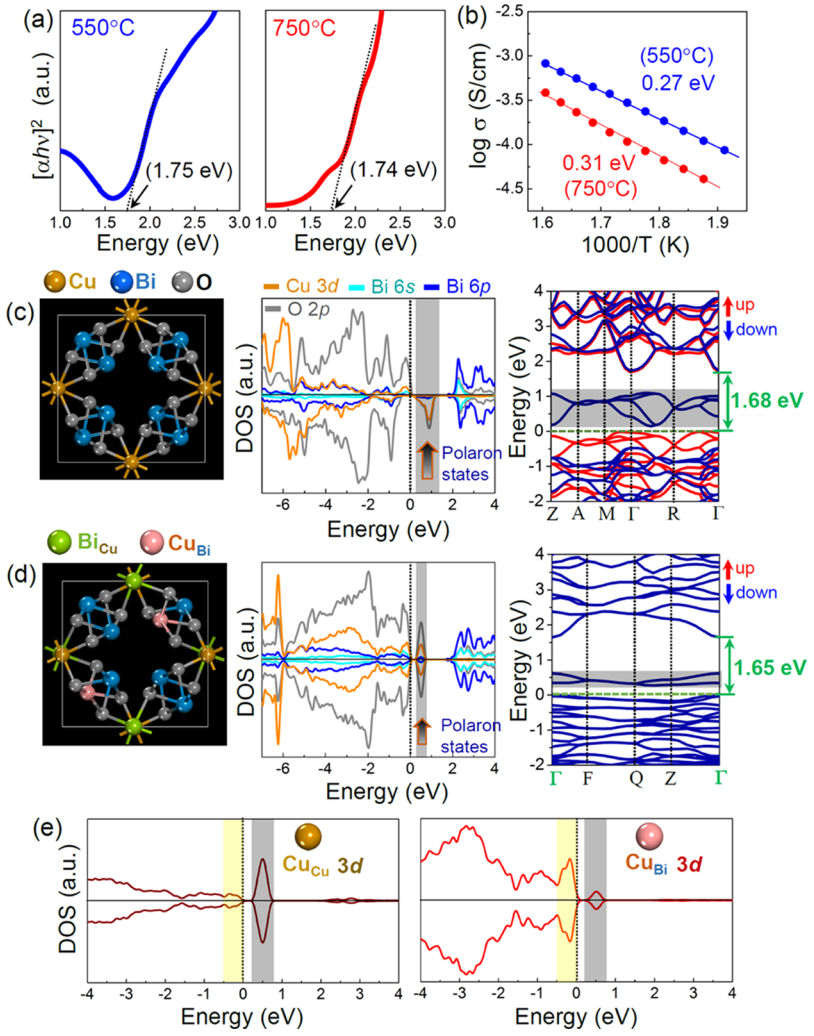

Figure 5. Measurements of optical and electrical properties and DFT calculations for electronic structure. (a) Dotted line in each of the Tauc plots derived from the optical absorbance indicates that the band gap is in the range of 1.70−1.75 eV in both samples. (b) Larger activation energy in addition to the lower conductivity values for the 750 °C sample is noted in this Arrhenius-type conductivity plot. (c, d) Density of states (DOS) and the electronic band structure from the DFT calculations are demonstrated for $CuBi_2O_4$ without intermixing (c) and with intermixing (d). The local polaron states within the band gap are indicated by black arrows along with gray shadows. (e) Distinct contributions of the Cu 3d stares between insite Cu_{Cu} (left) and antisite Cu_{Bi} (right) are demonstrated. A significantly small density from the antisite Cu_{Bi} 3d states is noted in the local polaron states (gray shadow), compared with the dominant contribution from the insite Cu_{Cu} 3d states.

CONCLUSIONS

We have directly visualized the presence of Bi_{Cu}−Cu_{Bi} antisite intermixing using both atomic-column-resolved imaging and chemical mapping in $CuBi_2O_4$ thin films. Based on the statistical and quantitative analysis on atomic columns of Cu and Bi, a substantial amount of intermixing was identified, showing a substantial degree of intermixing: 10% in terms of Cu sites in the 750 °C sample and 6% in the 550 °C sample, respectively. In addition, the local Cu 3d polaron states within the band gap were a notable feature acquired for the DFT calculations. The lower electronic conductivity and the higher activation energy in the Arrhenius plot observed in the 750 °C sample were thus reasonably suggested to stem from the hindrance by antisite Bi_{Cu} for hole-polaron hopping between Cu in the isolated square-planar configuration in a p-type $CuBi_2O_4$.

ASSOCIATED CONTENT

Supporting Information

The Supporting Information is available free of charge at https://pubs.acs.org/doi/10.1021/acsami.0c12491.

X-ray diffraction data, additional STEM images, additional EDS maps, and optical absorbance data (PDF)

Video clip for crystal structure (MP4)

AUTHOR INFORMATION

Corresponding Author

Sung-Yoon Chung − *Department of Materials Science and Engineering, Korea Advanced Institute of Science and Technology, Daejeon 34141, Korea;* orcid.org/0000-0002-2260-6201; Email: sychung@kaist.ac.kr

Authors

Hyun Joon Jung − *Department of Materials Science and Engineering and Graduate School of EEWS, Korea Advanced Institute of Science and Technology, Daejeon 34141, Korea*

https://dx.doi.org/10.1021/acsami.0c12491
ACS Appl. Mater. Interfaces 2020, 12, 43720−43727

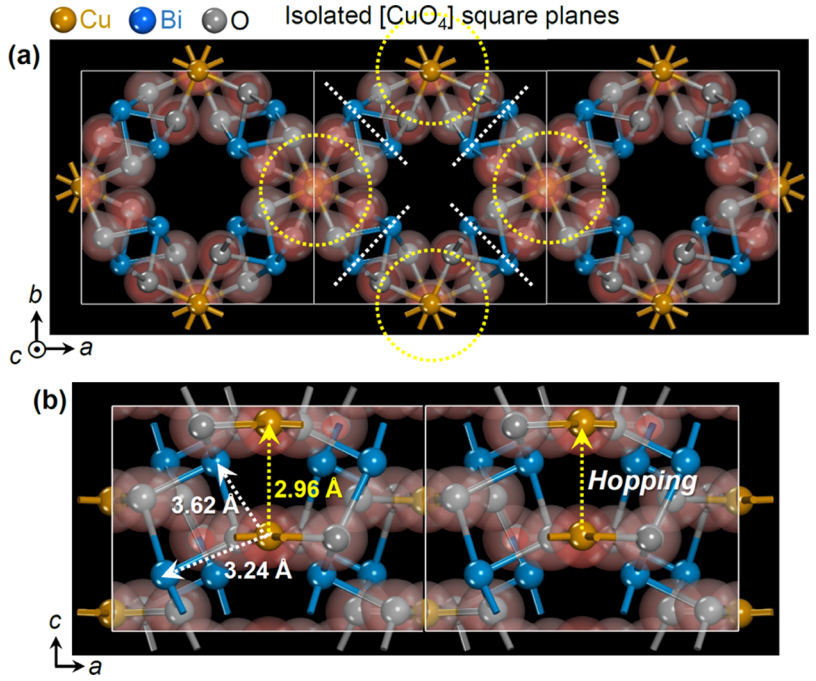

Figure 6. Isosurface contours showing an electron density difference field in pristine $CuBi_2O_4$. (a) Most electron-density field is contoured around Cu and O in the [CuO_4] square planes rather than Bi, as denoted by yellow circles. (b) This isosurface presentation in the *b*-axis projection also clarifies the confinement of the electron density in the [CuO_4] planes. The nearest cation of Cu is shown to be another Cu in the square planes along the *c*-axis. As a result, polaron hopping between the isolated [CuO_4] units along the *c*-axis is reasonably suggested to be a major conduction mechanism.

Younghwan Lim − *Department of Materials Science and Engineering, Korea Advanced Institute of Science and Technology, Daejeon 34141, Korea*
Byeong-Uk Choi − *Department of Materials Science and Engineering, Korea Advanced Institute of Science and Technology, Daejeon 34141, Korea*
Hyung Bin Bae − *KAIST Analysis Center, Korea Advanced Institute of Science and Technology, Daejeon 34141, Korea*
WooChul Jung − *Department of Materials Science and Engineering, Korea Advanced Institute of Science and Technology, Daejeon 34141, Korea;* orcid.org/0000-0001-5266-3795
Sangwoo Ryu − *Department of Advanced Materials Engineering, Kyonggi University, Suwon, Gyeonggi-do 16227, Korea;* orcid.org/0000-0002-9617-4958
Jihun Oh − *Department of Materials Science and Engineering, Korea Advanced Institute of Science and Technology, Daejeon 34141, Korea;* orcid.org/0000-0001-6465-6736

Complete contact information is available at: https://pubs.acs.org/10.1021/acsami.0c12491

Notes

The authors declare no competing financial interest.

■ ACKNOWLEDGMENTS

This work was supported by the National Research Foundation of Korea (NRF), grant numbers 2018R1A2B2006133 and 2019M3D1A2104100.

■ REFERENCES

(1) Walter, M. G.; Warren, E. L.; McKone, J. R.; Boettcher, S. W.; Mi, Q.; Santori, E. A.; Lewis, N. S. Solar Water Splitting Cells. *Chem. Rev.* **2010**, *110*, 6446−6473.
(2) Moniz, S. J. A.; Shevlin, S. A.; Martin, D. J.; Guo, Z.-X.; Tang, J. Visible-Light Driven Heterojunction Photocatalysts for Water Splitting − A Critical Review. *Energy Environ. Sci.* **2015**, *8*, 731−759.
(3) Sivula, K.; van de Krol, R. Semiconducting Materials for Photoelectrochemical Energy Conversion. *Nat. Rev. Mater.* **2016**, *1*, 15010.
(4) Tilley, S. D. Recent Advances and Emerging Trends in Photo-Electrochemical Solar Energy Conversion. *Adv. Energy Mater.* **2019**, *9*, 1802877.
(5) Lee, D. K.; Lee, D.; Lumley, M. A.; Choi, K.-S. Progress on Ternary Oxide-Based Photoanodes for Use in Photoelectrochemical Cells for Solar Water Splitting. *Chem. Soc. Rev.* **2019**, *48*, 2126−2157.
(6) Jang, Y. J.; Lee, J. S. Photoelectrochemical Water Splitting with p-Type Metal Oxide Semiconductor Photocathodes. *ChemSusChem* **2019**, *12*, 1835−1845.
(7) Fujishima, A.; Honda, K. Electrochemical Photolysis of Water at a Semiconductor Electrode. *Nature* **1972**, *238*, 37−38.
(8) Kim, T. W.; Choi, K. S. Nanoporous $BiVO_4$ Photoanodes with Dual-Layer Oxygen Evolution Catalysts for Solar Water Splitting. *Science* **2014**, *343*, 990−994.
(9) Rao, P. M.; Cai, L.; Liu, C.; Cho, I. S.; Lee, C. H.; Weisse, J. M.; Yang, P.; Zheng, X. Simultaneously Efficient Light Absorption and Charge Separation in WO_3/$BiVO_4$ Core/Shell Nanowire Photoanode for Photoelectrochemical Water Oxidation. *Nano Lett.* **2014**, *14*, 1099−1105.
(10) Wang, Y.; Tian, W.; Chen, C.; Xu, W.; Li, L. Tungsten Trioxide Nanostructures for Photoelectrochemical Water Splitting: Material Engineering and Charge Carrier Dynamic Manipulation. *Adv. Funct. Mater.* **2019**, *29*, 1809036.
(11) Rajeshwar, K.; Hossain, M. K.; Macaluso, R. T.; Janáky, C.; Varga, A.; Kulesza, P. J. Copper Oxide-Based Ternary and Quaternary Oxides: Where Solid-State Chemistry Meets Photoelectrochemistry. *J. Electrochem. Soc.* **2018**, *165*, H3192−H3206.
(12) Arai, T.; Konishi, Y.; Iwasaki, Y.; Sugihara, H.; Sayama, K. High-Throughput Screening Using Porous Photoelectrode for the Development of Visible-Light-Responsive Semiconductors. *J. Comb. Chem.* **2007**, *9*, 574−581.

(13) Arai, T.; Yanagida, M.; Konishi, Y.; Iwasaki, Y.; Sugihara, H.; Sayama, K. Efficient Complete Oxidation of Acetaldehyde into CO_2 Over $CuBi_2O_4/WO_3$ Composite Photocatalyst Under Visible and UV Light Irradiation. *J. Phys. Chem. C* **2007**, *111*, 7574−7577.
(14) Hahn, N. T.; Holmberg, V. C.; Korgel, B. A.; Mullins, C. B. Electrochemical Synthesis and Characterization of p-$CuBi_2O_4$ Thin Film Photocathodes. *J. Phys. Chem. C* **2012**, *116*, 6459−6466.
(15) Berglund, S. P.; Abdi, F. F.; Bogdanoff, P.; Chemseddine, A.; Friedrich, D.; van de Krol, R. Comprehensive Evaluation of $CuBi_2O_4$ as a Photocathode Material for Photoelectrochemical Water Splitting. *Chem. Mater.* **2016**, *28*, 4231−4242.
(16) Sharma, G.; Zhao, Z.; Sarker, P.; Nail, B. A.; Wang, J.; Huda, M. N.; Osterloh, F. E. Electronic Structure, Photovoltage, and Photocatalytic Hydrogen Evolution with p-$CuBi_2O_4$ Nanocrystals. *J. Mater. Chem. A* **2016**, *4*, 2936−2942.
(17) Kang, D.; Hill, J. C.; Park, Y.; Choi, K.-S. Photoelectrochemical Properties and Photostabilities of High Surface Area $CuBi_2O_4$ and Ag-Doped $CuBi_2O_4$ Photocathodes. *Chem. Mater.* **2016**, *28*, 4331−4340.
(18) Cao, D.; Nasori, N.; Wang, Z.; Mi, Y.; Wen, L.; Yang, Y.; Qu, S.; Wang, Z.; Lei, Y. p-Type $CuBi_2O_4$: An Easily Accessible Photocathodic Material for High-Efficiency Water Splitting. *J. Mater. Chem. A* **2016**, *4*, 8995−9001.
(19) Wang, F.; Septina, W.; Chemseddine, A.; Abdi, F. F.; Friedrich, D.; Bogdanoff, P.; van de Krol, R.; Tilley, S. D.; Berglund, S. P. Gradient Self-Doped $CuBi_2O_4$ with Highly Improved Charge Separation Efficiency. *J. Am. Chem. Soc.* **2017**, *139*, 15094−15103.
(20) Kim, N.-W.; Choi, B.-U.; Yu, H.; Ryu, S.; Oh, J. Formation of High-Density $CuBi_2O_4$ Thin Film Photocathodes with Polyvinylpyrrolidone-Metal Interaction. *Opt. Express* **2019**, *27*, A171−A183.
(21) Chung, S.-Y.; Choi, S.-Y.; Lee, S.; Ikuhara, Y. Distinct Configurations of Antisite Defects in Ordered Metal Phosphates: Comparison between $LiMnPO_4$ and $LiFePO_4$. *Phys. Rev. Lett.* **2012**, *108*, 195501.
(22) Chung, S.-Y.; Choi, S.-Y.; Kim, T.-H.; Lee, S. Surface-Orientation-Dependent Distribution of Subsurface Cation-Exchange Defects in Olivine-Phosphate Nanocrystals. *ACS Nano* **2015**, *9*, 850−859.
(23) Ryoo, H.; Bae, H. B.; Kim, Y.-M.; Kim, J.-G.; Lee, S.; Chung, S.-Y. Frenkel-Defect-Mediated Chemical Ordering Transition in a Li−Mn−Ni Spinel Oxide. *Angew. Chem., Int. Ed.* **2015**, *54*, 7963−7967.
(24) Chung, S.-Y.; Choi, S.-Y.; Yoon, H.-I.; Kim, H.-S.; Bae, H. B. Subsurface Space-Charge Dopant Segregation to Compensate Surface Excess Charge in a Perovskite Oxide. *Angew. Chem., Int. Ed.* **2016**, *55*, 9680−9684.
(25) Byeon, P.; Bae, H. B.; Chung, H.-S.; Lee, S.-G.; Kim, J.-G.; Lee, H. J.; Choi, J. W.; Chung, S.-Y. Atom-Scale Observation of $LiFePO_4$ and $LiCoO_2$ Dissolution Behavior in Aqueous Solutions. *Adv. Funct. Mater.* **2018**, *28*, 1804564.
(26) Bak, J.; Bae, H. B.; Chung, S.-Y. Atomic-Scale Perturbation of Oxygen Octahedra via Surface Ion Exchange in Perovskite Nickelates Boosts Water Oxidation. *Nat. Commun.* **2019**, *10*, 2713.
(27) Song, C. W.; Suh, H.; Bak, J.; Bae, H. B.; Chung, S.-Y. Dissolution-Induced Surface Roughening and Oxygen Evolution Electrocatalysis of Alkaline-Earth Iridates in Acid. *Chem* **2019**, *5*, 3243−3259.
(28) Zachman, M. J.; Hachtel, J. A.; Idrobo, J. C.; Chi, M. Emerging Electron Microscopy Techniques for Probing Functional Interfaces in Energy Materials. *Angew. Chem., Int. Ed.* **2020**, *59*, 1384−1396.
(29) Yoon, H.-I.; Lee, D.-K.; Bae, H. B.; Jo, G.-Y.; Chung, H.-S.; Kim, J.-G.; Kang, S.-J. L.; Chung, S.-Y. Probing Dopant Segregation in Distinct Cation Sites at Perovskite Oxide Polycrystal Interfaces. *Nat. Commun.* **2017**, *8*, 1417.
(30) Kim, H.-S.; Bae, H. B.; Jung, W.; Chung, S.-Y. Manipulation of Nanoscale Intergranular Phases for High Proton Conduction and Decomposition Tolerance in $BaCeO_3$ Polycrystals. *Nano Lett.* **2018**, *18*, 1110−1117.
(31) Rettie, A. J.; Chemelewski, W. D.; Emin, D.; Mullins, C. B. Unravelling Small-Polaron Transport in Metal Oxide Photoelectrodes. *J. Phys. Chem. Lett.* **2016**, *7*, 471−479.
(32) Ong, S. P.; Chevrier, V. L.; Ceder, G. Comparison of Small Polaron Migration and Phase Separation in Olivine $LiMnPO_4$ and $LiFePO_4$ Using Hybrid Density Functional Theory. *Phys. Rev. B* **2011**, *83*, 075112.
(33) Kweon, K. E.; Hwang, G. S.; Kim, J.; Kim, S.; Kim, S. Electron Small Polarons and Their Transport in Bismuth Vanadate: A First Principles Study. *Phys. Chem. Chem. Phys.* **2015**, *17*, 256−260.
(34) Zheng, J.; Teng, G.; Yang, J.; Xu, M.; Yao, Q.; Zhuo, Z.; Yang, W.; Liu, Q.; Pan, F. Mechanism of Exact Transition between Cationic and Anionic Redox Activities in Cathode Material Li_2FeSiO_4. *J. Phys. Chem. Lett.* **2018**, *9*, 6262−6268.
(35) Pan, H.; Meng, X.; Liu, D.; Li, S.; Qin, G. (Ti/Zr, N) Codoped Hematite for Enhancing the Photoelectrochemical Activity of Water Splitting. *Phys. Chem. Chem. Phys.* **2015**, *17*, 22179−22186.
(36) Carneiro, L. M.; Cushing, S. K.; Liu, C.; Su, Y.; Yang, P.; Alivisatos, A. P.; Leone, S. R. Excitation-Wavelength-Dependent Small Polaron Trapping of Photoexcited Carriers in α-Fe_2O_3. *Nat. Mater.* **2017**, *16*, 819−825.
(37) Lohaus, C.; Klein, A.; Jaegermann, W. Limitation of Fermi Level Shifts by Polaron Defect States in Hematite Photoelectrodes. *Nat. Commun.* **2018**, *9*, 4309.
(38) Chung, S.-Y.; Choi, S.-Y.; Yamamoto, T.; Ikuhara, Y. Orientation-Dependent Arrangement of Antisite Defects in Lithium Iron(II) Phosphate Crystals. *Angew. Chem., Int. Ed.* **2009**, *48*, 543−546.
(39) Kim, H.-S.; Jang, A.; Choi, S.-Y.; Jung, W.; Chung, S.-Y. Vacancy-Induced Electronic Structure Variation of Acceptors and Correlation with Proton Conduction in Perovskite Oxides. *Angew. Chem., Int. Ed.* **2016**, *55*, 13499−13503.
(40) Kim, J.-H.; Choi, S.-Y.; Choi, M.; Gershon, T.; Lee, Y. S.; Wang, W.; Shin, B.; Chung, S.-Y. Atomic-Scale Observation of Oxygen Substitution and Its Correlation with Hole-Transport Barriers in $Cu_2ZnSnSe_4$ Thin-Film Solar Cells. *Adv. Energy Mater.* **2016**, *6*, 1501902.
(41) Jesson, D.; Pennycook, S. Incoherent Imaging of Thin Specimens Using Coherently Scattered Electrons. *Proc. R. Soc. London, Ser. A* **1993**, *441*, 261−281.
(42) Nolan, M.; Elliott, S. D. The p-Type Conduction Mechanism in Cu_2O: A First Principles Study. *Phys. Chem. Chem. Phys.* **2006**, *8*, 5350−5358.
(43) Ekuma, C.; Anisimov, V.; Moreno, J.; Jarrell, M. Electronic Structure and Spectra of CuO. *Eur. Phys. J. B* **2014**, *87*, No. 23.
(44) Mishra, A. K.; Roldan, A.; de Leeuw, N. H. CuO Surfaces and CO_2 Activation: A Dispersion-Corrected DFT+U Study. *J. Phys. Chem. C* **2016**, *120*, 2198−2214.

https://dx.doi.org/10.1021/acsami.0c12491
ACS Appl. Mater. Interfaces 2020, 12, 43720−43727